Nakajima *Earth, Planets and Space* (2023) 75:48
https://doi.org/10.1186/s40623-023-01807-6

Earth, Planets and Space

FULL PAPER

Open Access

The Wakayama earthquake swarm in Japan

Junichi Nakajima*

Abstract

An earthquake swarm in the Wakayama prefecture, Japan, is known as the most active and persistent swarm, with > 95,000 earthquakes ($M \geq -1.3$) occurring during the 2003–2020 period. However, no systematic studies have highlighted the source of this intriguing non-volcanic earthquake swarm to date. This study systematically investigates the temporal and spatial evolution of the Wakayama earthquake swarm and estimates the seismic velocity structure around the Kii peninsula, where we observe series of anomalous geophysical and geochemical signatures, such as high $^{3}He/^{4}He$ ratios, deep low-frequency earthquakes, and hot springs with high salinity and solute concentrations. We reveal that seismicity associated with the Wakayama earthquake swarm occurs almost evenly in both time and space, and that the majority of the earthquakes in the northern part of the swarm activity occur along well-defined planes that dip to the west at 30–45°. The seismic tomography results reveal that a northwestward-dipping low-velocity zone exists beneath the Wakayama swarm and the low-velocity zone is sandwiched by high-velocity anomalies in the continental crust interpreted as impermeable and rigid materials on both sides in the subduction direction. This unique tectonic setting controls a pathway of the upward migration of slab-derived fluids to the surface, with the high fluid concentration in the dipping low-velocity zone. Therefore, we infer that the location of the Wakayama swarm is controlled by deep crustal heterogeneities rather than by the major structures of geological accretionary complexes. This study suggests that the anomalous geophysical and geochemical signatures observed across the Kii peninsula are different manifestations of the frictional and hydrological processes during the upward migration of the slab-derived fluids. We further propose that the valley-shaped geometry of the Philippine Sea slab beneath the Kii peninsula is caused by the rigid materials in the continental crust.

Keywords Philippine Sea plate, Travel-time tomography, Fluids, Low-frequency earthquakes

*Correspondence:
Junichi Nakajima
nakajima@geo.titech.ac.jp
Full list of author information is available at the end of the article

Graphical Abstract

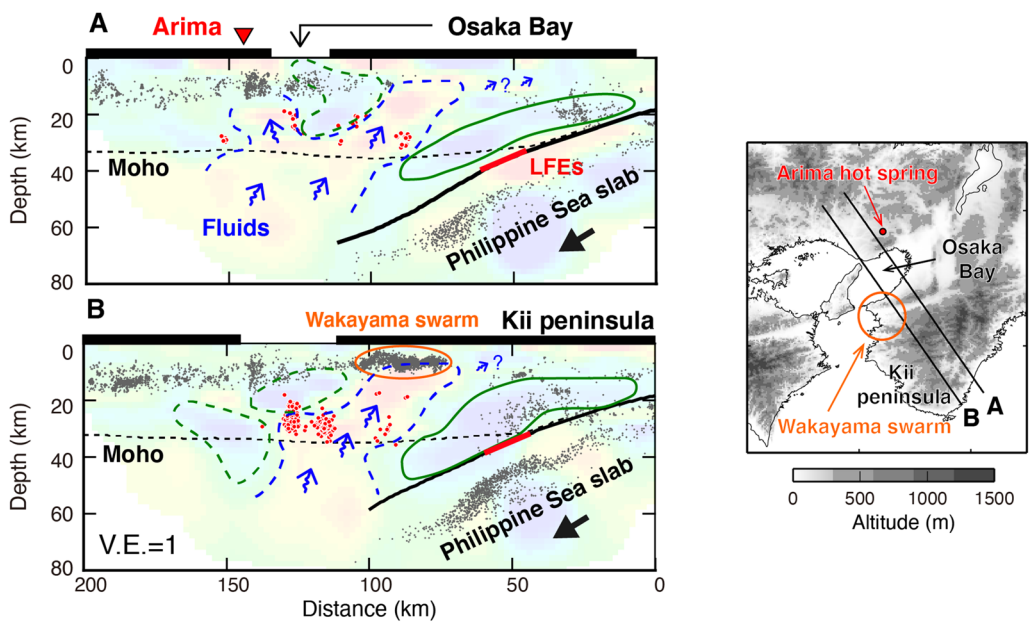

Introduction

Earthquakes are often classified into two types: mainshock–aftershock sequences and swarms. A mainshock–aftershock sequence generally starts with the largest earthquake (mainshock) in the sequence (smaller preshocks may sometimes precede the mainshock), followed by a series of smaller aftershocks that cease over time. The aftershock activity generally obeys the Omori law, whereby the decay in aftershock activity follows a power law. Conversely, an earthquake swarm occurs in a confined area and consists of a number of successive similar-magnitude earthquakes, with no observations of clear mainshock. Swarm activity usually starts with no distinct seismic signals, lasts from months to years, and is often observed in volcanic and geothermal fields (e.g., Chen and Shearer 2011; Shelly et al. 2013) and near the vicinity of anthropogenic fluid injection wells (e.g., Keranen et al. 2014). The most famous swarm in Japan is the Matsushiro earthquake swarm in a volcanic area of central Japan; it started in August 1965, with >60,000 felt earthquakes during the ~5-year swarm period (e.g., Mogi 1988). However, there are earthquake swarms, or concentrated seismicity, in non-volcanic areas that are characterized by >100 years of persistent seismicity (e.g., Yoshida and Takayama 1992).

An earthquake swarm in the Wakayama prefecture (hereafter called the Wakayama earthquake swarm) is the most active and persistent non-volcanic earthquake swarm in Japan (Fig. 1) (e.g., Mizoue et al. 1983; Kato et al. 2010; Yoshida et al. 2011). The Wakayama swarm possesses a very high rate of background seismicity (e.g., Yoshida and Takayama 1992) and occurs over a 30 km × 30 km area (e.g., Maeda et al. 2018). The swarm is located immediately south of the Median Tectonic Line (MTL), the largest active fault in Japan, which divides the southwestern Japan into the inner and outer arcs (Fig. 1). The spatial correlation between this swarm location and the local geological units has previously been investigated, and geological faults that act as weak planes have been interpreted as a major cause of this earthquake swarm (Maeda et al. 2018, 2021). However, the MTL and other major geological units extend farther to the west and east of the Wakayama region (e.g., Isozaki et al. 1990; Geological Survey of Japan, AIST 2022), and the reason for the confined location of this earthquake swarm remains elusive.

Here we systematically investigate the Wakayama earthquake swarm in the period of 2003–2020 using the unified earthquake catalog of the Japan Metrological Agency (JMA) ($M \geq 0$; $N = 81{,}875$) to elucidate the cause of this intriguing swarm activity. This study first provides an overview of the tectonic framework of ongoing plate subduction, then investigates the temporal and spatial characteristics of the earthquake swarm. The three-dimensional (3D) seismic velocity structure to a depth of 60 km is estimated to discuss the heterogeneous crustal

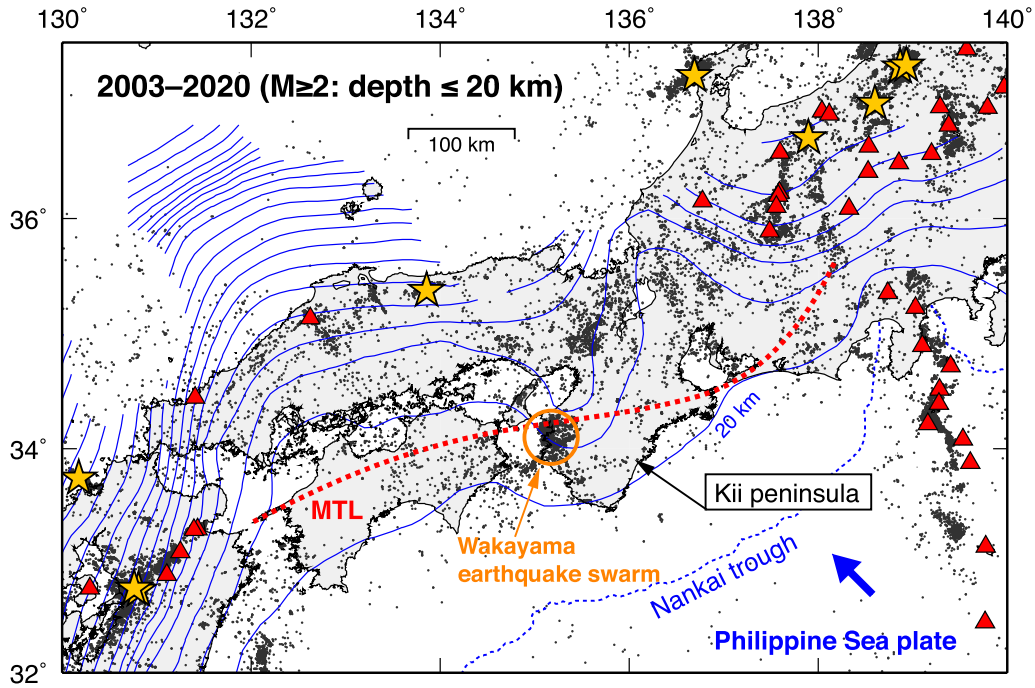

Fig. 1 Tectonic framework of western Japan. Blue solid denote the iso-depth contours of the Philippine Sea (PHS) slab at a 20-km interval (Hua et al. 2018, and references therein). Red triangles and orange stars represent active volcanoes and $M \geq 6.5$ crustal earthquakes that occurred during the 2003–2020 period, respectively. Dots indicate the $M \geq 2$ earthquakes that occurred at 0–20 km depth. The Median Tectonic Line (MTL), which divides southwestern Japan into the inner and outer arcs, is shown by the dashed red line. Blue dashed lines denote the location of the Nankai trough

and uppermost mantle structure around the Wakayama swarm. We provide a comprehensive interpretation of the seismic observations and propose that the rigid crustal materials above the Philippine Sea (PHS) plate serve as a structural control on the upward migration of slab-derived fluids. The presence of the rigid materials is interpreted as an essential cause of the Wakayama earthquake swarm and other distinct geophysical and geochemical phenomena, such as deep low-frequency earthquakes (LFEs), emanation of high $^3He/^4He$ ratios, and the discharge of the Arima-type brine across the Kii peninsula.

The Wakayama earthquake swarm

Tectonic framework of ongoing plate subduction

The Wakayama earthquake swarm (orange circle in Fig. 1) is located beneath the Kii peninsula, which is a non-volcanic area in southwestern Japan, and has had a high rate of persistent background seismicity for the past ~100 years (e.g., Yoshida and Takayama 1992). The PHS plate is subducting northwestward beneath the Wakayama swarm at a rate of 3–4 cm/year, and a valley-like shape of the PHS slab is formed beneath the Kii peninsula. The depth to the upper interface of the PHS slab beneath the swarm is ~40 km (Figs. 1 and 2).

The Wakayama earthquake swarm occurs in a limited 30 km × 30 km area (Maeda et al. 2018) and is bounded by areas with limited shallow crustal seismicity (Fig. 2a). Here, we define the area of the Wakayama swarm by the rectangle in Fig. 2a (33.85–34.35° N, 135–135.5° E, and 0–20 km depth). The focal depths of the eartqhuake swarm are locally shallower than the earthquakes in the surrounding areas (Fig. 2b). Deep LFEs, whose signals are dominated by < 8 Hz energy, occur in the continental crust at ~30 km depth to the north of the Wakayama swarm (gray dots along profile B in Fig. 2). It is likely that fluids are distributed beneath the area of LFEs, as LFEs are interpreted as being facilitated by the accumulation of fluids or magma near the Moho (e.g., Aki and Koyanagi 1981; Hasegawa and Yamamoto 1994; Aso et al. 2013; Oikawa et al. 2021).

Earthquake depth distribution and *b* values

Figure 3a highlights the depth distributions for crustal earthquakes ($M \geq 1$) in the Wakayama swarm and the surrounding areas (areas outside of the rectangle in Fig. 2a). The depth distribution for the earthquake swarm is notably different from that for the earthquakes in the surrounding areas, with the focal depths of the earthquake swarm (6.9 ± 1.9 km) being ~5 km shallower than

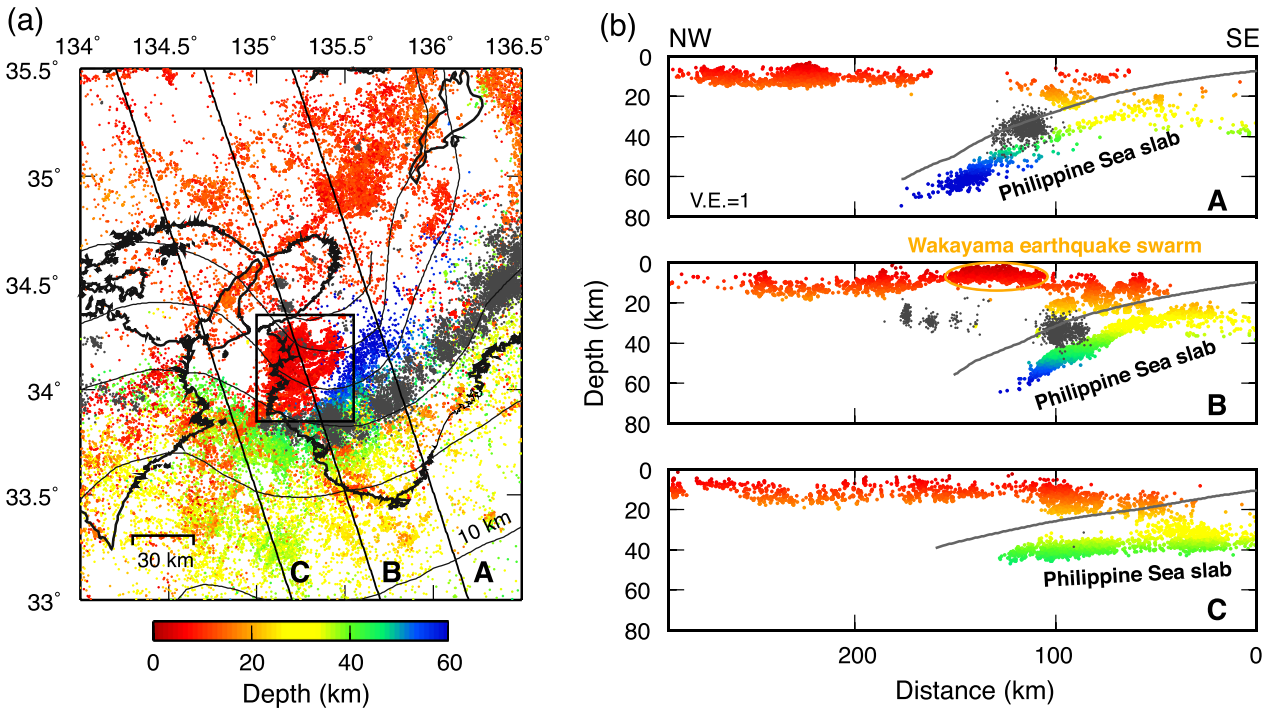

Fig. 2 Seismicity around the Wakayama earthquake swarm. **a** Map showing the $M \geq 1$ earthquake distribution, with the focal depths color-coded. Gray dots denote low-frequency earthquakes. Black contours denote the iso-depth contours of the PHS slab at a 10-km interval. The rectangle denotes the Wakayama swarm. **b** Vertical cross sections of the earthquakes within ± 10 km from the three profiles in (**a**). The Wakayama earthquake swarm is shown by an orange ellipse in profile B. The upper surface of the PHS slab is shown by the gray line in each cross section

those for the other earthquakes (11.8 ± 2.8 km) on average. This suggests that the hypocenters of the swarm are exceptionally shallow, and that such shallow focal depths are probably related to the cause of this earthquake swarm.

We estimated the b values from the magnitude–frequency distributions for the earthquakes at 0–20 km depth in the Wakayama swarm and the surrounding areas. To estimate the optimal cutoff magnitude, M_c, we first calculated R values, which represent the absolute difference of the number of earthquakes in each magnitude bin between the observed and synthetic distributions (Wiemer and Wyss 2000), and confirmed that R values are higher than 95% for $M_c \geq 0.8$ for both areas. We obtained stable b values of 0.95–0.96 for the Wakayama swarm and 0.93–0.94 for the surrounding areas with $M_c = 0.8$–1.0. The magnitude–frequency distributions and b values estimated with $M_c = 1.0$ are shown in Fig. 3b. The estimated b values are consistent with those obtained for crustal earthquakes in the southwestern Japan (e.g., Oth 2013). The Wakayama swarm is, therefore, not distinct from other crustal earthquakes based on its magnitude–frequency distribution, even though the focal depths are significantly shallower.

Spatial distribution of the Wakayama swarm

Detailed hypocenter maps of the Wakayama earthquake swarm are shown in Fig. 4. We observed an overall homogeneous epicentral distribution of the $M \geq 0$ earthquakes, with the exception of a few spots and lineaments, where there are absence of seismicity (dashed circles and arrows, respectively, in Fig. 4a). The hypocenters are shallow (~4 km depth) in the northern part of the swarm area (at ~34.2° N and ~135.2° E) and deepen to ~10 km depth to the west and south. The focal depths in the eastern part of the swarm, at ~135.4° E, are variable, ranging from 5 km at ~34.1° N to ~10 km at ~34.3° N. The $M \geq 1$ and $M \geq 2$ earthquake distributions are rather scattered compared with the $M \geq 0$ distribution, but the overall pattern of seismicity is unchanged (Fig. 4b, and c). Marked NE–SW bands of seismicity are seen in the central to southern parts of the swarm. We observed twelve $M \geq 4$ earthquakes during the 2003–2020 analyzed period, with four concentrated in the area with the shallow focal depths (at ~34.2° N and ~135.2° E).

The focal mechanism solutions for the Wakayama swarm, which have been determined by the JMA for the $M \geq 3$ earthquakes, show that reverse-type focal mechanisms with N–S striking nodal planes are predominantly observed, together with a small number of

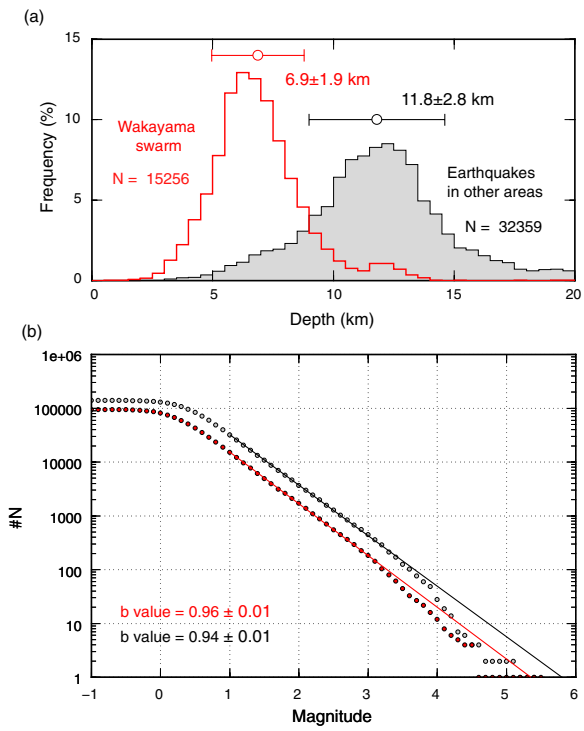

Fig. 3 **a** Frequency distribution of the focal depths of earthquakes in the Wakayama swarm (red) and in the areas surrounding the Wakayama swarm (gray). The hypocenter distributions are shown in Fig. 2a. Average focal depths and their associated standard deviations are indicated by the circle and error bars, respectively. **b** Magnitude–frequency distribution of the earthquakes in the Wakayama swarm (red) and in the surrounding areas of the Wakayama swarm (gray). Estimated *b* values for the $M \geq 1$ earthquakes are shown

strike-slip-type focal mechanisms with the E–W-oriented *P*-axes. These results suggest that the E–W-oriented compressional stress regime is dominant in the earthquake swarm. However, the N–S striking nodal planes of the focal mechanisms are not consistent with the ENE–WSW strikes of the major geological faults in the region (e.g., Isozaki et al. 1990; Geological Survey of Japan 2022), suggesting that $M \geq 3$ earthquakes occur along fault planes that have different orientations from the major geological faults. In contrast, Maeda et al. (2018) investigated the focal mechanisms of the smaller earthquakes ($M \geq 1.1$) and found that $M < 2.5$ earthquakes have variable focal mechanisms with 31% of the analyzed mechanisms being classified as strike-slip or normal faulting. Since smaller strike-slip earthquakes in the southern part of the earthquake swarm area have a nodal plane that is sub-parallel to the ENE–WSW strike of the major geological faults, Maeda et al. (2018) concluded that these earthquakes occur along sub-vertical weak faults with the strike of the ENE–WSW direction.

Temporal distribution of the Wakayama swarm

We investigated the temporal characteristics of the swarm activity during the 2003–2020 period. A magnitude–time plot for the $M \geq 1$ earthquakes demonstrates that the swarm consists of small- to moderate-size earthquakes, with twelve $M \geq 4$ earthquakes (including one $M \geq 5$ earthquake) occurring over the 18-year analysis period (Fig. 5a). The largest earthquake (M5.5) occurred on July 5, 2011, 4 months after the M9 Tohoku–oki earthquake. Figure 5b shows that the seismicity rate is semi-constant, with only minor fluctuations during the analysis period.

The average seismicity rate in the earthquake swarm was estimated to be 2.3 per day from 15,256 earthquakes ($M \geq 1$) over the 18-year period (black dashed straight line in Fig. 5b). To better characterize the temporal variations in the seismicity rate of the earthquake swarm, we calculated the cumulative number of earthquakes that are deviated from the average seismicity rate as $\Delta N = \sum_i (N_i - 2.3)$, where N_i is the number of earthquakes in *i*th day. Figure 5c shows that ΔN slightly fluctuates with time. The seismicity rate was higher than the average until ~2006, but then dropped below the average in 2007–2010. The seismicity rate increased again after the concentrated occurrences of three $M \geq 4$ earthquakes in 2011 and then decreased almost monotonically until the end of 2020. The seismicity rate was sometimes enhanced after the occurrence of each $M \geq 4$ earthquakes, which may correspond to the increased seismicity associated with each mainshock–aftershock sequence in the swarm activity.

We plotted the hypocenter distributions for the January–February earthquakes for each year, as an example, to show spatial variations in seismicity (Fig. 6). The earthquakes are distributed in very similar locations with almost an identical number of earthquakes for each 2-month period. We confirmed that the hypocenter distributions in other 2-month or 1-month periods show almost identical patterns, thereby indicating that there were little regional variations in the observed seismicity over 18 years. These observations suggest that the earthquakes in the Wakayama swarm occur almost evenly in both time and space.

We found that the seismicity rate increased over a short time scale of less than 2 months in the beginning of 2004, when no $M \geq 4$ earthquakes occurred (Fig. 5c). This increase is associated with the initiation of an isolated seismicity in the southernmost part of the study area at ~12 km depth (blue arrow in the 2004 panel in Fig. 6). This earthquake cluster was activated on December 10, 2003 and had ceased by late February 2004. Although such an abrupt activation of a specific earthquake cluster is interesting and warrants for further investigation,

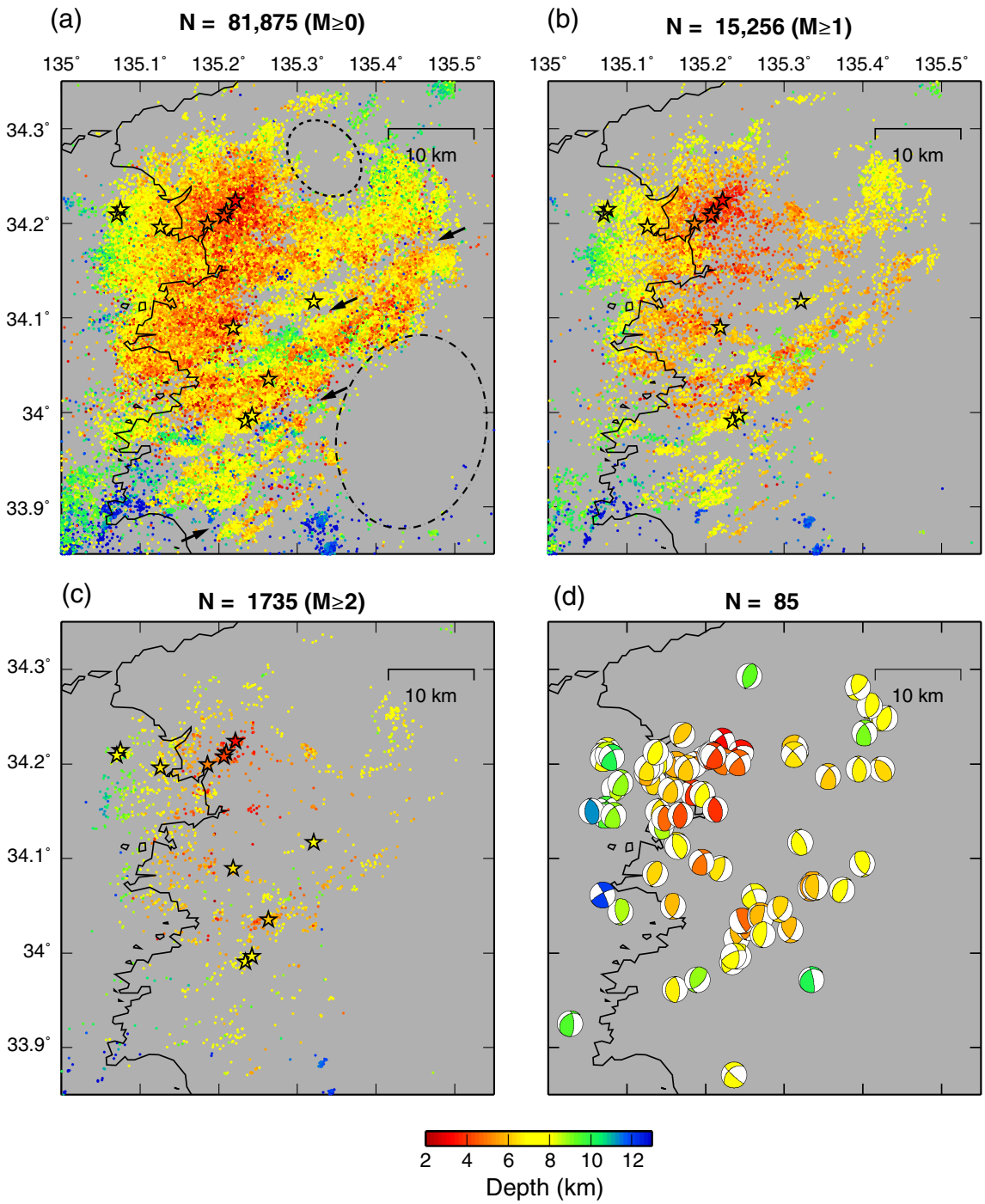

Fig. 4 Hypocenter distributions of the Wakayama swarm during the 2003–2020 period. **a** $M \geq 0$ earthquakes. **b** $M \geq 1$ earthquakes. **c** $M \geq 2$ earthquakes. Dashed ellipses and arrows in (**a**) denote areas and lineaments with limited seismicity, respectively. Stars in (**a**–**c**) denote $M \geq 4$ earthquakes. Focal depths are color-coded. **d** Focal mechanism solutions for the $M \geq 3$ earthquakes that are reported in the JMA catalog

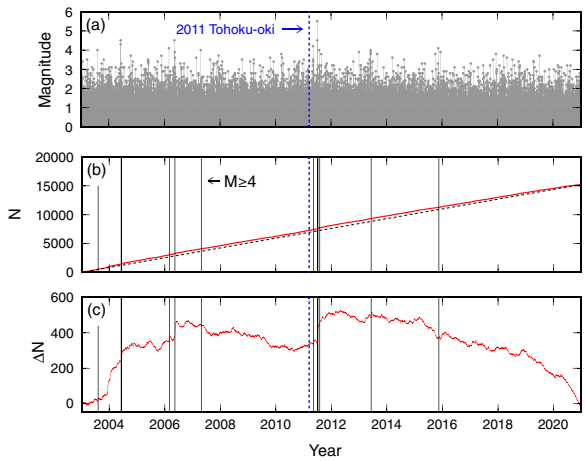

Fig. 5 **a** Magnitude–time plot for the $M \geq 1$ earthquakes in the Wakayama swarm. The blue vertical line denotes the timing of the 2011 Tohoku–oki earthquake. **b** Cumulative number of $M \geq 1$ earthquakes (red line). The black dashed line denotes an average seismicity rate of 2.3 earthquakes per day (15,256 earthquakes over the 18-year analysis period). Vertical lines indicate when the $M \geq 4$ earthquakes occurred in the swarm. **c** Cumulative number (ΔN) of $M \geq 1$ earthquakes deviated from the average seismicity rate. It is noted that ΔN becomes zero at both ends of the analyzed period

the origin of this cluster is not discussed further here, as this cluster does not represent the main seismicity of the Wakayama swarm which is the focus of this study.

Hypocenter relocation

We relocated hypocenters with hypoDD (Waldhauser and Ellsworth 2000) to better delineate the hypocenter distributions. We first relocated hypocenters reported in the JMA catalog for the 2003–2020 period using the catalog-derived differential travel-time data to constrain the overall earthquake distribution of the Wakayama swarm. This analysis considered all of the $M \geq 1$ earthquakes and calculated the earthquake pairs with inter-event distances of < 10 km at 58 stations that are located within epicentral distances of < 100 km. We obtained the total number of 3,346,861 P-wave and 2,788,482 S-wave differential travel-time data from 15,142 earthquakes.

The relocated hypocenters indicate that the earthquakes form a tighter distribution within the swarm compared with the JMA locations (Fig. 7); however, the overall pattern of seismicity is unchanged. The

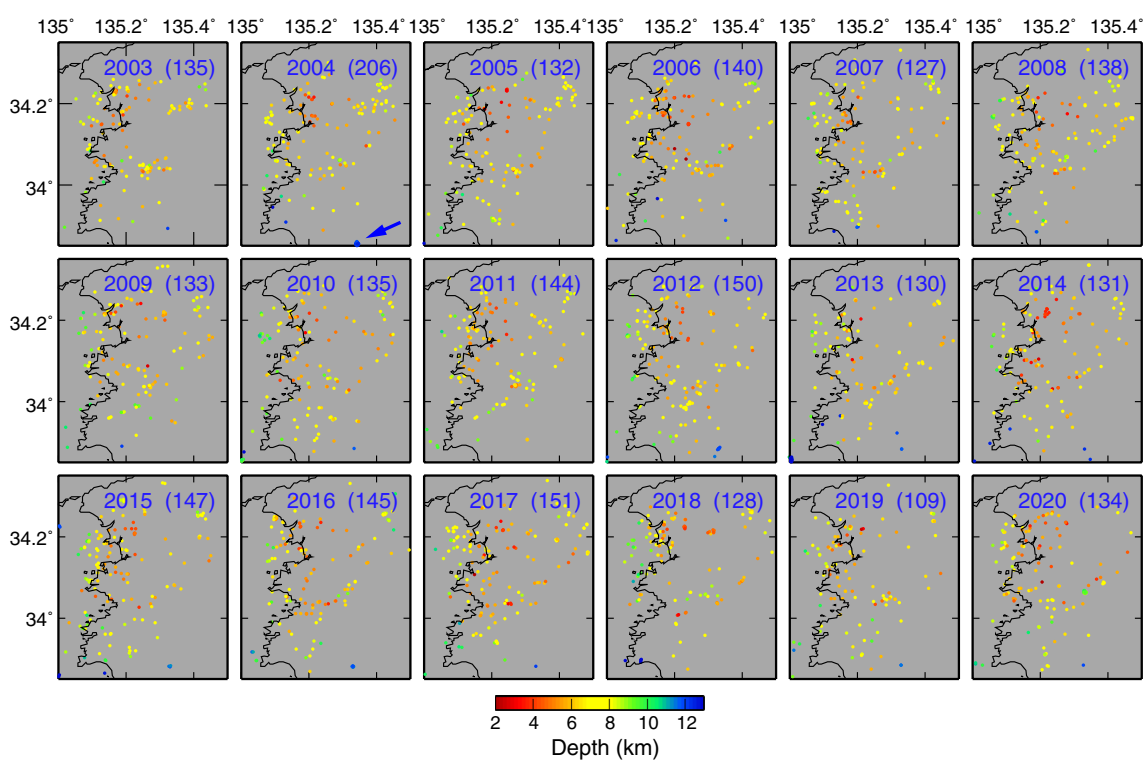

Fig. 6 Hypocenter distributions of the January–February events for each year in the analysis period (2003–2020). The number of recorded earthquakes in each 2-month period is shown in parentheses. Focal depths are color-coded. The blue arrow in 2004 marks the seismicity that is discussed in the text

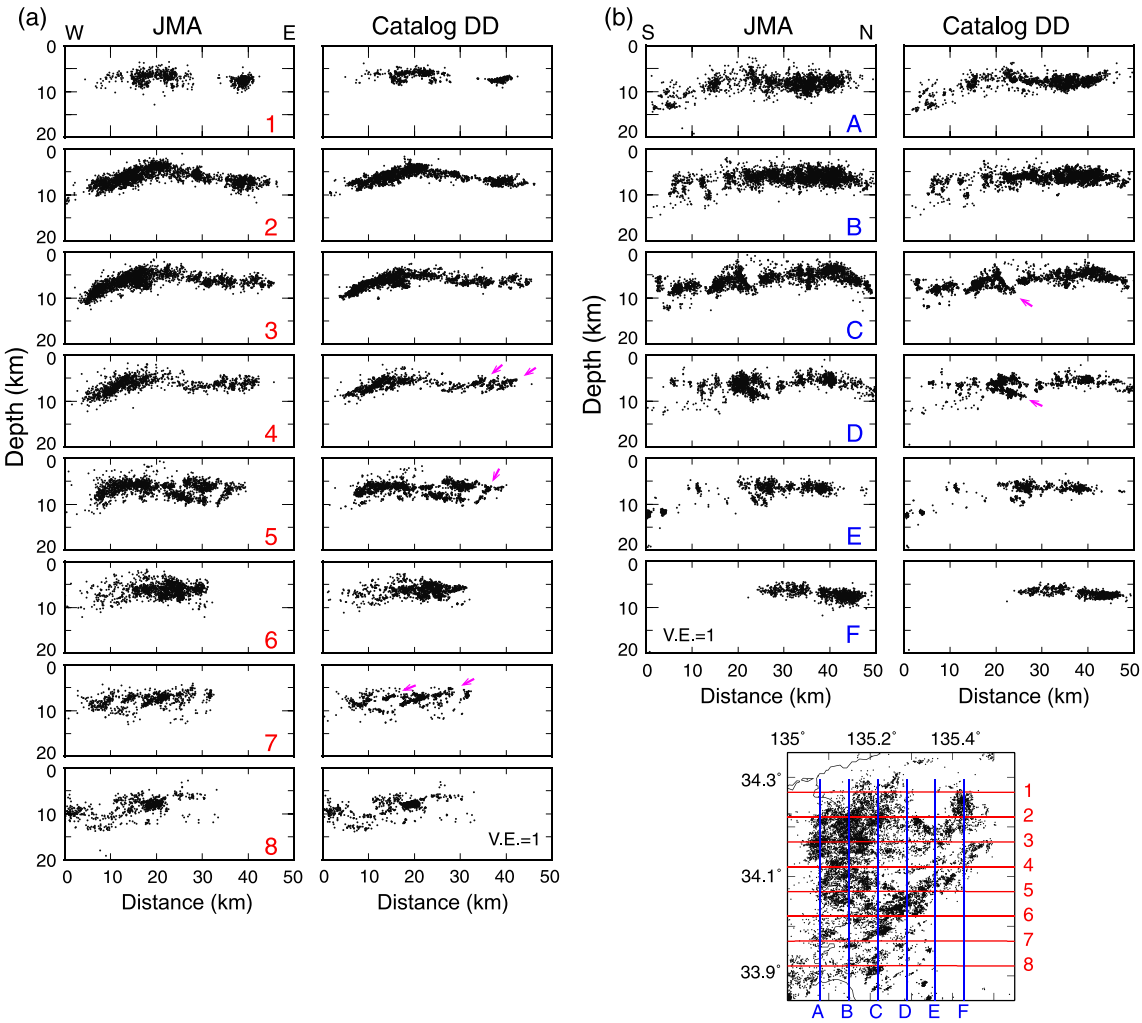

Fig. 7 Vertical cross sections of the (left) JMA hypocenters and (right) relocated hypocenters using the catalog-derived differential time data. **a** E–W vertical cross sections. **b** N–S vertical cross sections. Purple arrows denote distinct seismicity dipping northwestward. Profile locations are shown on the inset map. E–W profiles are spaced at a 0.05° (~5.5 km) interval, and N–S profiles are spaced at a 0.07° (~6.3 km) interval. The earthquakes in each profile do not appear in the adjacent profiles

earthquakes projected along the E–W cross sections form a convex distribution in the northern part of the swarm (profiles 2–4 in Fig. 7a), whereas the hypocenters in the southern part are distributed sub-horizontally (profiles 5–8 in Fig. 7a). The thickness of the hypocenter distribution is thin in the northern part compared with that in the southern part. Although a convex hypocenter distribution is discernible along the N–S vertical cross sections (profiles C and D in Fig. 7b), this pattern is less clear compared with the hypocenter distribution along the E–W cross sections. It appears that some of the earthquakes in the southern part occurred in isolated clusters, as shown in the N–S vertical cross sections (horizontal distances of 0–20 km in Fig. 7b). In addition, the hypocenters in the southeastern part of the swarm are distributed along several distinct planes dipping northwestward (purple arrows in profiles 4, 5, 7, C, and D in Fig. 7). These results suggest that the earthquake swarm consists of three segments, with highly concentrated, convex distribution of hypocenters in the northwestern part, more isolated, tiny earthquake clusters in the southern part, and northwestward dipping earthquakes in the southeastern part.

We further relocated the hypocenters using waveform-derived differential travel-time data to characterize the hypocenter distributions at a much finer scale. The cross-spectral method was applied to both P and S waves to calculate arrival-time differences for the $M \geq 1$ earthquake pairs with inter-event distances of < 3 km. The arrival-time differences and coherence values of

each earthquake pair were calculated from the vertical component for the P waves and the transverse component for the S waves in the 2–12 Hz frequency band of a given 2-s time window that began 0.2 s before the onset of each phase. In the relocation, we included the arrival-time differences with a coherency of ≥ 0.8 at 28 stations that are located within epicentral distances of < 50 km. The relocated hypocenters from the catalog-based hypoDD results were used as the initial hypocenters for this waveform-based hypoDD approach. We obtained 9522 relocated hypocenters with the waveform-derived differential time data.

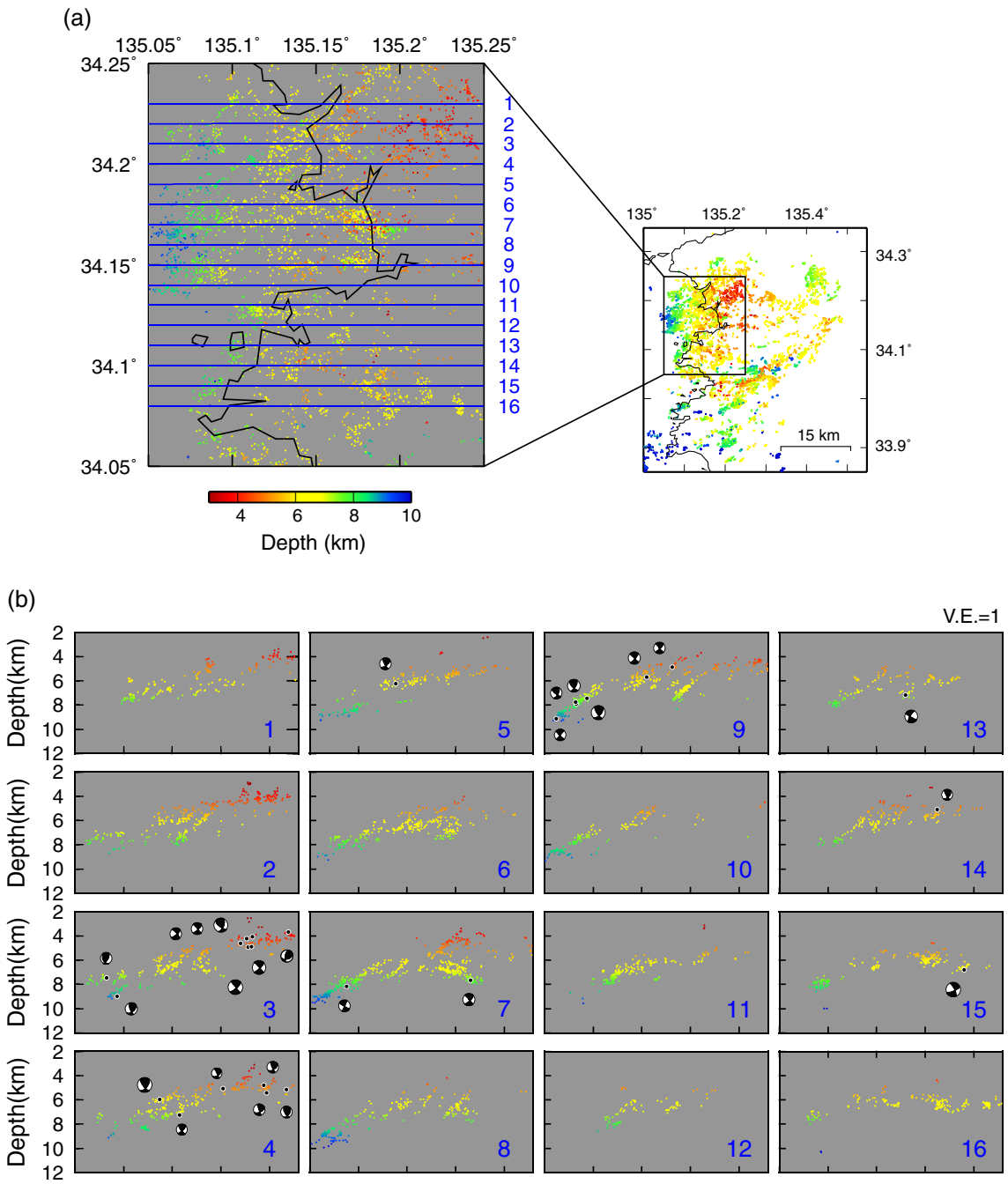

Fig. 8 **a** Distribution of the hypocenters that were relocated using waveform-derived differential time data. Focal depths are color-coded. The map location is indicated on the inset map. **b** E–W vertical cross sections of the hypocenters. The focal mechanism solutions of the $M \geq 3$ earthquakes that are reported in the JMA catalogue are shown. Profiles are spaced at a 0.01° (~ 1.1 km) interval, and the earthquakes in each profile do not appear in the adjacent profiles

Here we focus on the hypocenter distributions in the northwestern part of the swarm, where seismic activity is high and seismicity dips to the west (Fig. 7). Figure 8 shows the hypocenter relocation results along 16 E–W trending profiles that are spaced at a 0.01° (~1.1 km) interval, which can highlight the westward dipping seismicity of the convex distribution. The relocated hypocenters with waveform-based hypoDD reveal small-scale structures in the swarm activity. For example, a majority of the hypocenters along profile 9 align along well-defined, sub-parallel planes that dip to the west at 30–45°, and the dip of the planes are consistent with one of the nodal planes of focal mechanism solutions. The characteristic lengths of these well-defined alignments of seismicity are 3–4 km with thickness of ≤1 km. Interestingly, we observe a different orientation of the earthquake alignments along profile 7, which dip to the east at ~30°. This suggests that a conjugate fault system is partly developed in the northern part of the Wakayama swarm, even though the overall trend of the fault structures is westward dipping. Our high-resolution hypocenter relocations reveal that finer-scale, multi-layered seismic fault systems are well-developed within the earthquake swarm area, with each earthquake occurring along an individual fault plane within a complex fault system.

Three-dimensional seismic velocity structures

Data and methods

We carried out a 3D travel-time tomography analysis to elucidate the structural heterogeneity around the Wakayama earthquake swarm. We set the model space to span a volume of ~140 km × ~330 km × 80 km (33.2–35.5° N, 134°–137° E, and 0–80 km depth). We used the P- and S-wave arrival-time data for $M \geq 1$ earthquakes ($N = 62{,}333$) that occurred during the 2003–2020 period and were documented in the JMA catalog (Additional file 1: Figure S1a); this resulted in 1,321,037 and 1,277,961 P- and S-wave phase data, respectively, which were recorded at 154 seismograph stations across the study area (squares in Additional file 1: Figure S1b). Most of the stations that were located above the Wakayama swarm possessed ~30,000 ray paths for the P-wave data (Additional file 1: Figure S1b).

The tomographic method of Zhao et al. (1992) was used to estimate the 3D seismic velocity structure. We set horizontal grid nodes with 0.15° (~15 km) spacing around the Wakayama earthquake swarm and 0.2° (~20 km) spacing in the surrounding areas and vertical ones at 0, 5, 10, 15, 20, 25, 30, 40 60, and 80 km depth (Additional file 1: Figure S1b). We adopted the initial 1D P-wave velocity model that was constructed from the JMA 2001 velocity model (Ueno et al. 2002) and calculated 1D S-wave velocity model using a constant V_p/V_s value of 1.73. We introduced a priori information for two crustal discontinuities: the Conrad and Moho discontinuities (Katsumata 2010). The geometry of the PHS slab was not prescribed in the model space. The root mean squares of the P-wave and S-wave arrival-time residuals were reduced from 0.20 to 0.12 s and from 0.27 to 0.16 s, respectively, after five iterations.

We conducted two checkerboard resolution tests (CRTs) with different parameterizations to assess the reliability of the obtained velocity images. We assigned velocity perturbations of ±10% either to alternate grid nodes or to every two grid nodes and calculated the travel times, respectively, for the two models to produce synthetic arrival-time data. We added random noise to the synthetic data with standard deviations of 0.05 and 0.10 s for P waves and S waves, respectively, which correspond to the phase-picking errors. We then inverted the synthetic arrival-time data using the same earthquake–station geometry and model parameterizations as in the real inversion. The results of the two CRTs are shown Additional file 2: Figure S2. The checkerboard patterns of the alternate grid node are recovered considerably in the southern part of the Kii peninsula to 40 km depth, but they are not well-recovered beneath the earthquake swarm at 15 and 20 km depth (Additional file 2: Figure S2a). Conversely, the checkerboard patterns that were assigned to every two grid nodes show a better recovery beneath the earthquake swarm, even though the checkerboard patterns are smeared at 15 and 20 km depth (Additional file 2: Figure S2b). The CRTs results demonstrate that our data set can resolve the heterogeneous structures in the crust and the uppermost mantle over horizontal scales of >15–20 km in the southern part of the Kii peninsula and of >20–30 km beneath the Wakayama earthquake swarm.

Results

The obtained P- and S-wave velocity perturbations and V_p/V_s ratios at 10, 15, 20, 30, 40, and 60 km depth are shown in Fig. 9 (see Additional file 3: Figure S3 for the absolute velocity images). The velocity perturbations (in %) are the deviations from the average P- and S-wave velocities at each depth. We observe an E–W trending low-velocity anomaly along the MTL at 10 km depth, which becomes more distinct at 15 and 20 km depth. The low-velocity anomaly associated with the MTL has been highlighted in previous studies (e.g., Omuralieva et al. 2012) and is interpreted as a fluid-rich area. The V_p/V_s values are overall low (<1.70) at 10 and 15 km depth, whereas V_p/V_s values of >1.8 are observed at 20–60 km depth around the Osaka Bay. A large, distinct high-velocity anomaly is distributed across the southern part of the Kii peninsula at 15 and 20 km depth (indicated by white

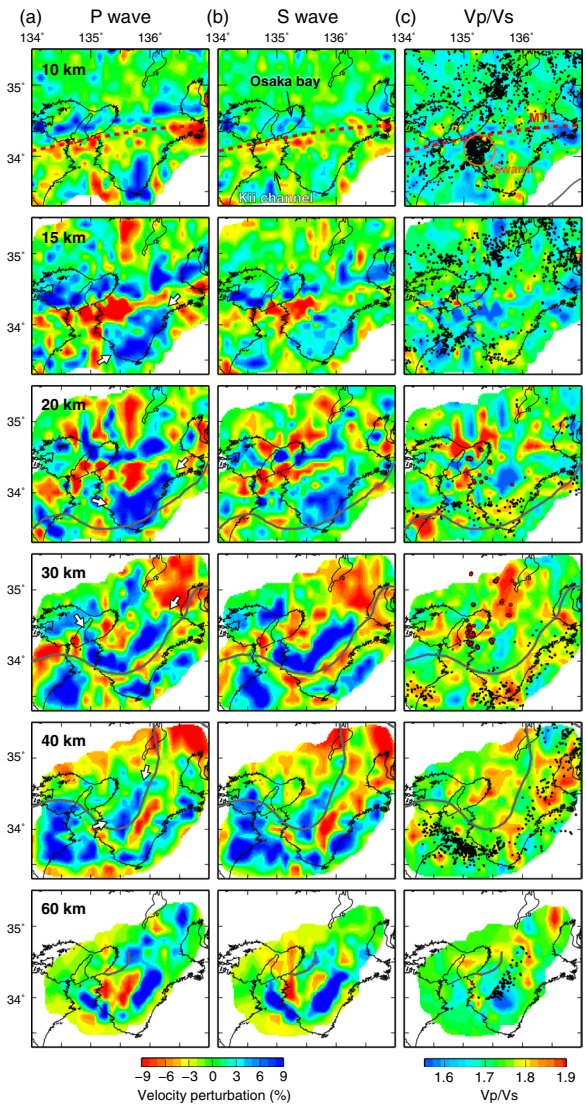

Fig. 9 **a** P-wave and **b** S-wave velocity perturbations and **c** V_p/V_s ratios at 10, 15, 20, 30, 40, and 60 km depth. Velocity perturbations are the deviations from the average velocity at each depth. Gray curves represent the iso-depth contour of the PHS slab at each depth. Regions with a deviated weight sum of > 1000 are shown. Hypocenter (black dots) and LFE (red circles) distributions are shown in (**c**) (note that tectonic LFEs are not shown). White arrows at 15–40 km depth in (**a**) denote the high-velocity zone discussed in the text

arrows in Fig. 9a). This high-velocity anomaly is located within the continental plate above the slab owing to its continent-ward position relative to the iso-depth contour of the PHS slab. The high-velocity anomaly persists at 30–40 km depth, exhibits the same curvature as the iso-depth contour of the PHS slab, and shifts northwestward with increasing depths. These features suggest that the high-velocity anomaly overlies the PHS slab at 15–40 km depth. The V_p/V_s values for the high-velocity anomaly are moderate (1.7–1.8) at each depth.

The observed velocity anomalies are further characterized along the vertical cross sections in Fig. 10, which are the profiles sub-parallel to the subduction of the PHS slab (see Additional file 4: Figure S4 for the absolute velocity images). The PHS slab is subducting beneath the Kii peninsula from the southeast, where we observe inclined seismicity that corresponds to intraslab earthquakes. A distinct, thin, low-velocity layer is distributed immediately below the upper surface of the PHS slab down to ~40 km depth (profiles A–C) and is interpreted as the hydrated subducting crust (e.g., Hirose et al. 2008; Kato et al. 2014). We note that the PHS slab does not possess a continuous high-velocity anomaly (profiles A–E), which is atypical for the subducting slab mantle. The absence of a high-velocity anomaly that corresponds to the slab mantle has also been highlighted in previous studies (e.g., Seno et al. 2001; Nakajima and Hasegawa 2007a, b) and has been attributed to the high degree of hydration of the slab mantle.

The marked high-velocity zone immediately above the PHS slab is well-visualized at horizontal distances of 0–80 km along profiles A–E (Fig. 10) and possesses a thickness of ~20 km. This northwestward dipping high-velocity zone was partly revealed by Salah and Zhao (2003), and its upper boundary has been imaged as a distinct velocity boundary via receiver function analyses (e.g., Yamauchi et al. 2003; Kato et al. 2014). Conversely, a distinct low-velocity anomaly exists at 10–40 km depth beneath the Wakayama swarm (profiles D–F in Fig. 10). This low-velocity zone dips northwestward and has been partly imaged in the previous studies as an area with high intrinsic and scattering attenuation (e.g., Matsunami and Nakamura 2004; Petukhin and Tagawa 2007; Kita and Matsubara 2016). The deep LFEs that occur in the lower crust beneath the Osaka Bay are located around this low-velocity zone. Interestingly, another high-velocity zone appears to exist to the northwest of the inclined low-velocity zone beneath or to the northwest of the Osaka Bay at 10–30 km depth (horizontal distances of 120–170 km along profiles C–G). Therefore, the northwestward-dipping low-velocity zone beneath the Wakayama swarm is sandwiched by the two high-velocity anomalies along the direction of the PHS slab subduction. The V_p/V_s values of the low-velocity zone beneath the Wakayama swarm are low (< 1.7) in the middle crust and are high (> 1.8) in the lower crust and the uppermost mantle.

Discussion

Structural controls on the earthquake swarm location

The most striking feature of the tomographic results is the presence of a northwestward-dipping, three-layered

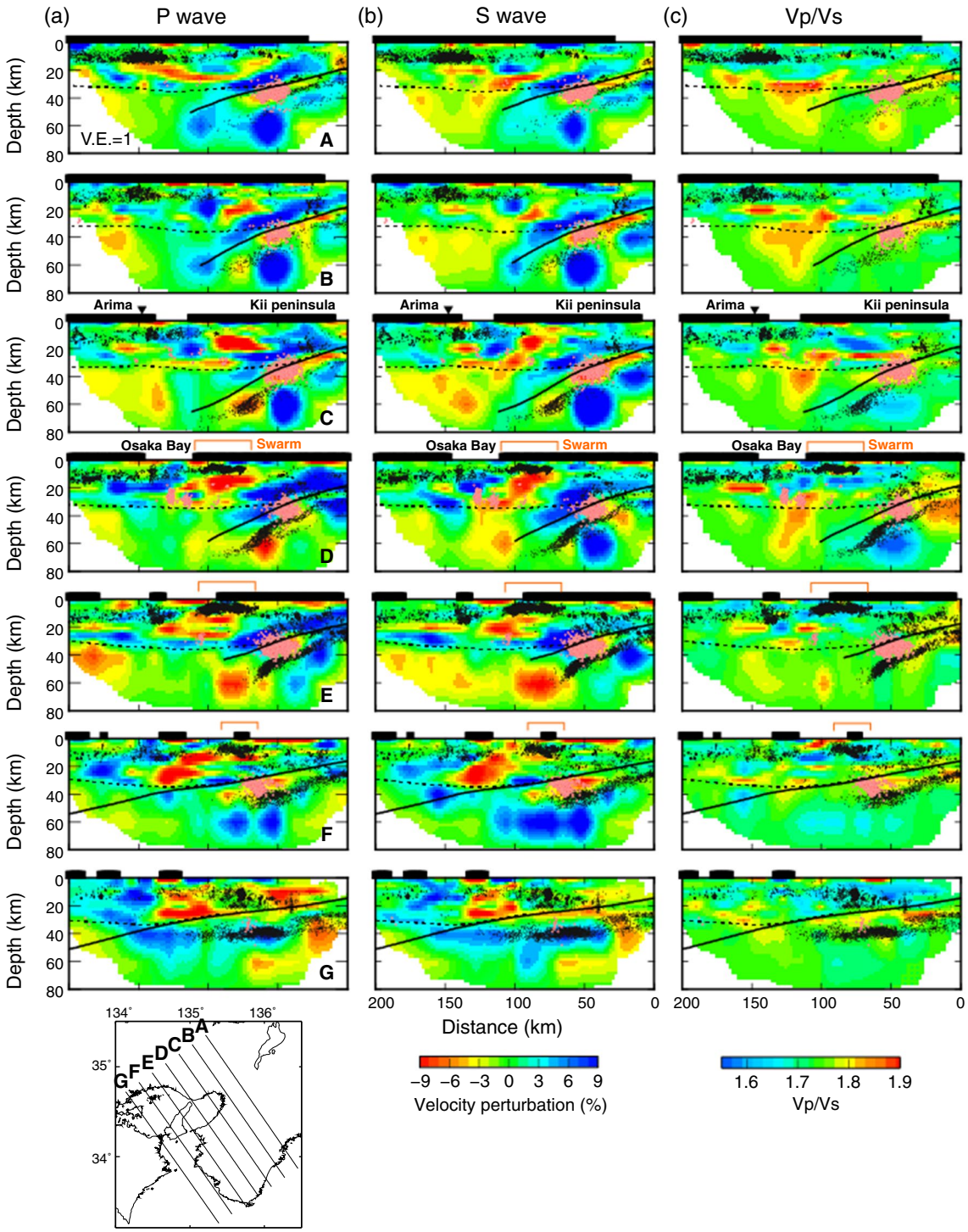

Fig. 10 Vertical cross sections of the **a** P-wave and **b** S-wave velocity perturbations and **c** V_p/V_s ratios along the seven profiles (A–G) shown on the inset map. Black dots and red circles denote the earthquakes and LFEs, respectively, within a 5-km-wide zone along each profile. Black dashed and black solid lines denote the Moho (Katsumata 2010) and upper surface of the PHS slab (Nakajima and Hasegawa 2007b; Hirose et al. 2008), respectively. Black bars on the surface represent the land areas

structure above the PHS slab at least at 10–40 km depth, which consists of a distinct high-velocity anomaly immediately above the PHS slab, a low-velocity anomaly beneath the Wakayama swarm, and a high-velocity anomaly beneath the Osaka Bay (Fig. 10). Uehara et al. (2005) revealed that a high-density and high-resistivity zone exists above the PHS slab down to at least ~30 km depth in the southwestern part of the Kii peninsula and interpreted the zone to be a pluton of acidic rocks. We infer that the inclined high-velocity anomaly imaged above the PHS slab corresponds to the high-density and high-resistivity zone and interpret the zone to be a body of impermeable and rigid materials. The inferred locations of the impermeable and rigid materials are enclosed by the green curves in Fig. 11a, and b, where the observed velocity anomalies are higher than ~5%.

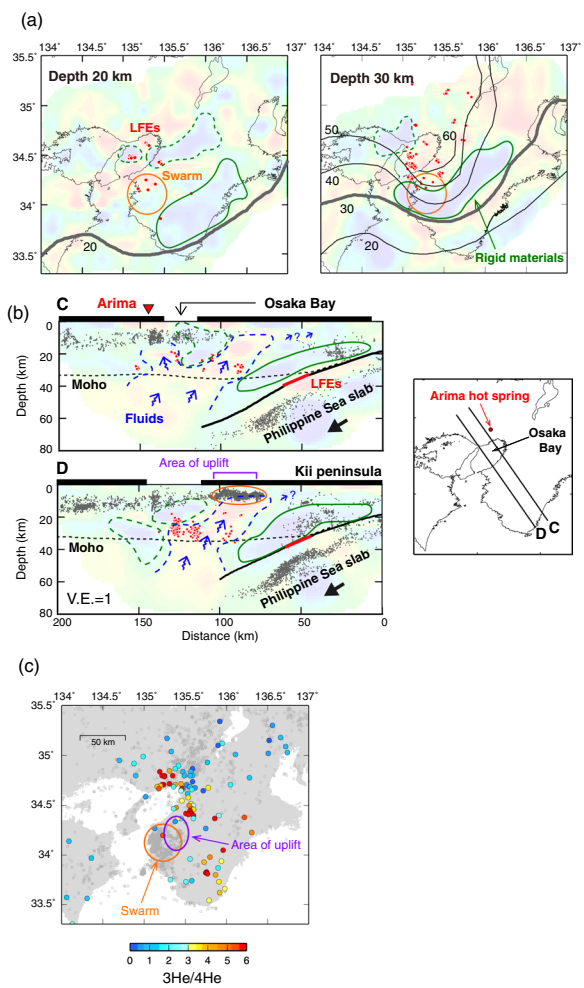

Fig. 11 Interpretation of the velocity structures **a** for two depth slices and **b** along two across-arc vertical cross sections. The Wakayama swarm is shown by an orange circle in the depth slices and an orange ellipse in the vertical cross section. Green areas are interpreted to be rigid and impermeable materials. See the text for further details. **c** Distribution of the air-corrected $^3He/^4He$ ratios (Sano and Wakita 1985; Matsumoto et al. 2003; Umeda et al. 2007; Sano et al. 2009; Morikawa et al. 2016). The purple ellipse denotes an area of uplift at >4 mm/year (Yoshida et al. 2011)

The presence of the impermeable, rigid materials above the PHS slab is consistent with the interpretation of Nakajima and Hasegawa (2016), whereby impermeable materials act as a cap layer and prevent effective drainage from the subducting slab to the overlying plate. The tectonic LFEs along the megathrust boundary are probably enhanced immediately below the impermeable materials (Figs. 10 and 11), where pore-fluid pressures along the megathrust boundary can be elevated to near-lithostatic values. It is noted that the mantle-wedge corner beneath the Kii peninsula has been suggested to be serpentinized (e.g., Kato et al. 2014), but our tomographic results do not support a serpentinized mantle wedge, because the high-velocity anomaly (V_p of >8 km/s and V_s of >4.5 km/s; Additional file 4: Figure S4) and moderate V_p/V_s values (~1.75) in this area are not indicative of serpentinization (Christensen 1996; Watanabe et al. 2007).

The high-velocity anomaly beneath the Osaka Bay has similar seismic characteristics (high velocity of >5% and low to moderate V_p/V_s values) (profiles B–D in Fig. 10) to the northwestward-dipping high-velocity zone above the PHS slab that we interpreted to be the impermeable, rigid materials. Therefore, we infer that the high-velocity anomaly beneath the Osaka Bay also represents rigid materials that have been minimally influenced by fluids or thermal anomalies (areas enclosed by green dashed curves in Fig. 11a, b). Most importantly, the inferred locations of the two rigid materials are limited to the Kii peninsula and Osaka Bay and appear to bound both the Wakayama swarm and deep LFE areas (Fig. 11a). The two zones of rigid materials probably control the upward migration of slab-derived fluids to the surface, thereby forcing the fluids to localize along an inherent permeable zone that is sandwiched by the impermeable materials. We interpret that the permeable zone is imaged as a distinct, northwestward-dipping low-velocity zone and that large amounts of fluids can migrate toward the Wakayama swarm through this permeable zone. This hypothesis strongly suggests that the location of the Wakayama swarm is controlled by the structural heterogeneities in the crust.

Although the origin of the rigid and impermeable materials above the PHS slab remains elusive, we infer that the rigid materials correspond either to the root of acidic rocks known as the Kumano pluton (e.g., Arnulf et al. 2022) or to old and stagnant rocks that have not been heavily metamorphosed by slab-derived fluids, despite the subduction of the PHS slab over the last 15

Myr. Notably, the lateral extent of the inferred rigid materials immediately above the PHS slab coincides with that of the steep, valley-shaped subduction of the PHS slab (Fig. 11a). We interpret that the existence of the rigid, stagnant materials in the continental crust may have blocked the gently dipping subduction of the PHS slab and forced the PHS slab to subduct at steeper angles, as suggested by Arnulf et al. (2022). This hypothesis can explain the valley-shaped geometry of the PHS slab that is locally developed only beneath the Kii peninsula.

High ^{3}He/^{4}He ratios, LFEs, and Arima-type hot springs

There are several anomalous geochemical and geophysical observations around the Kii peninsula. Sano and Wakita (1985) revealed that anomalously high ^{3}He/^{4}He ratios of up to 8 Ra (Ra, the atmospheric ^{3}He/^{4}He ratio) are observed across the Kii peninsula. Subsequently, it was confirmed that the observations of such high ^{3}He/^{4}He ratios are not limited to the Kii peninsula but also extend along an NNW–SSE-oriented elongated area that extends from the southern part of the Kii peninsula to the north of the Osaka Bay (Fig. 11c) (e.g., Matsumoto et al. 2003; Umeda et al. 2007; Sano and Nakajima 2008; Sano et al. 2009; Morikawa et al. 2016). Another notable observation is an Arima-type brine, whose oxygen and hydrogen isotope compositions are similar to those of magmatic/metamorphic fluids (e.g., Matsubaya et al. 1973). The origin of this Arima hot spring has been long argued, since the Arima hot spring is far from any volcanic sources. Furthermore, the Osaka Bay is an exceptional area in Japan where isolated, deep LFEs occur in non-volcanic environment (Figs. 9 and 11). Aso et al. (2011) showed that the overall pattern of LFE spectrum beneath Osaka Bay is similar to that of volcanic LFEs and suggested that the Osaka Bay LFEs are related to fluids accumulation near the Moho.

The anomalous geochemical and geophysical observations in this non-volcanic area have been interpreted as indicators of either the upward migration of PHS slab-derived fluids (e.g., Matsumoto et al. 2003; Umeda et al. 2007) or fluids expulsion from a shallow magma body or solidified magmas (e.g., Sano and Wakita 1985; Kato et al. 2014). The results of this study suggest that aqueous fluids, rather than magma or partial melts, are likely to exist in the upper crust beneath the Wakayama swarm, because the observed low-velocity and low-V_p/V_s values (<1.7) cannot be explained by the presence of magma or melts (e.g., Nakajima et al. 2001; Takei 2002). Conversely, the low-velocity and high-V_p/V_s values (>1.8) observed at 20–40 km depth can be attributed to either magma (partial melts) or aqueous fluids (e.g., Takei 2002). Although we cannot discriminate the cause of this low-velocity anomaly from seismological observations alone, the Wakayama swarm and Arima hot spring are both in non-volcanic areas (100–150 km away from the nearest Quaternary volcano) and the terrestrial heat flow in this region is not extremely high as that in volcanic areas (Tanaka et al. 2004). Therefore, we infer that the low-velocity and high-V_p/V_s values in the lower crust represent the existence of fluids rather than magma or partial melts.

Kusuda et al. (2014) suggested that the high salinity and solute concentrations of the Arima-type hot springs can be explained by dehydration of the PHS slab, because the estimated ^{87}Sr/^{86}Sr ratio of the deep brine is closer to the estimated ratio of PHS slab-derived fluids rather than that of Pacific slab-derived fluids. Crustal dehydration reactions of the PHS slab have been inferred to occur at either 15–50 km (Yamasaki and Seno 2003), or 32–44 km (Yoshioka et al. 2008), or ~60 km (Peacock 2009) depth, whereas the mantle dehydration reactions are expected at 25–75 km depth (Yamasaki and Seno 2003). Although the inferred depth ranges of these dehydration reactions are less constrained due to large uncertainties in the thermal structure of the PHS slab, it is evident that PHS slab-derived fluids are potentially expelled to the overlying plate over a broad depth range, where intraslab earthquakes occur (e.g., Hasegawa and Nakajima 2017).

We infer that PHS slab-derived fluids are supplied to the uppermost mantle beneath the Osaka Bay and are the primary origin of the anomalous geophysical and geochemical observations across the Kii peninsula. Our observations suggest that slab-derived fluids first trigger deep LFEs beneath the Osaka Bay, then they migrate upward toward the Wakayama area along the permeable zone, eventually facilitating the Wakayama earthquake swarm in the seismogenic upper crust and producing the high ^{3}He/^{4}He ratios across the Kii peninsula. We speculate that the fluids migrating toward the Wakayama swarm are being further supplied to the southern part of the peninsula through potential permeable pathways above the impermeable materials (small blue arrows in Fig. 11b), even though this study cannot resolve such fine-scale structures. In contrast, the location of Arima hot spring is consistent with the location of a branch of the permeable zone, which facilitates upward fluid migration toward Arima hot spring, as illustrated in Fig. 11b. The high salinity and solute concentrations and high ^{3}He/^{4}He ratios observed around the Arima hot spring are likely a result of the supply of the slab-derived fluids. Therefore, we conclude that the anomalous geophysical and geochemical signatures that have been observed across the Kii peninsula arise from a common source, and the observed variations are caused by different manifestations of the frictional and hydrological processes of the concentrated supply of slab-derived fluids.

Earthquake triggering along pre-existing faults

Our observations have revealed that the hypocenters in the northern part of the Wakayama swarm are aligned along well-defined planes that dip to the west at 30–45° (Fig. 8), which demonstrates that the earthquakes occur along individual fault planes. The focal mechanisms of $M \geq 3$ earthquakes are consistent with the occurrences of earthquakes along westward-dipping fault planes with the strike of the N–S direction. Since the strikes of the major geological faults around the Wakayama swarm are oriented almost in the ENE–WSW direction, we interpret that the earthquakes in the northern part of the Wakayama swarm are triggered not by the reactivation of the major geological units but by shear fault slip of westward-dipping faults that are preferably activated as reverse faulting under the regional E–W compressional stress regime (e.g., Terakawa and Matsu'ura 2010; Uchide et al. 2022). It is noted, however, that small strike-slip earthquakes in the southwestern part of the Wakayama swarm that have ENE–WSW-oriented nodal planes (Maeda et al. 2018) may occur along the major geological faults or their branches striking the ENE–WSW direction. This study does not detail the genesis of isolated, tiny earthquake clusters observed in the southern part, and we would require additional studies to discuss their origin.

Yoshida et al. (2011) found that the vertical uplift of up to 10 mm/year has occurred immediately to the east of the Wakayama swarm and suggested that the uplift is caused by the intrusion of volcanic rocks beneath the eastern part of the swarm region (a purple ellipse in Fig. 11c). Maeda et al. (2018) proposed the existence of a heat source beneath the Wakayama swarm to explain the depth-dependent stress regime of the observed for small earthquakes in Wakayama. However, our tomographic results show that a specific heat source, such as magmatic body or solidified magma, with a dimension larger than ~15 km is unlikely to be present beneath the Wakayama swarm. Therefore, we infer that the migration of a large amount of the slab-derived fluids to near the surface is related to the observed vertical uplift of ~10 mm/year, even though the horizontal offset between swarm activity and the area of uplift remains unsolved.

We propose, based on recent experiments and observations, and that three essential processes must occur to generate the earthquake swarm (Danré et al. 2022; Nakajima and Hasegawa 2023). First, a large volume of overpressurized fluids originating from slab-derived fluids migrate upward, and infiltrate into individual faults in the upper crust (Fig. 12). High pore-fluid pressures can then stabilize shear slip along the rate-strengthening part (creep areas) of each fault by increasing the friction parameter (a–b) and reducing the critical stiffness (k_c)

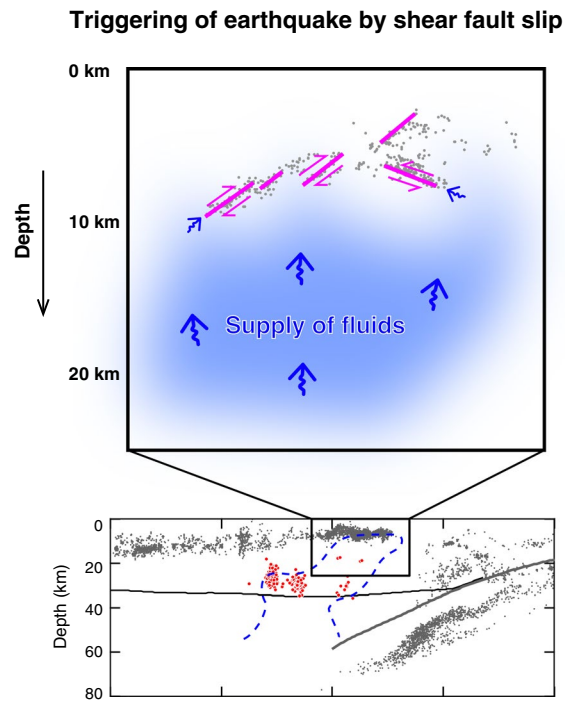

Fig. 12 Schematic cartoon of the upward migration of slab-derived fluids to the seismogenic zone and their infiltration into individual faults. Earthquake swarm is triggered by shear slip along individual faults

(e.g., Scholz 1998; Cappa et al. 2019; Bedford et al. 2021), which may trigger aseismic slip along pre-existing faults. These high pore-fluid pressures can simultaneously cause a reduction in the shear strength of the frictionally locked asperity patches on each fault. The combination of enhanced aseismic slip and the weakened strength of asperity patches may have triggered the persistent seismicity that is recognized as an earthquake swarm. We consider that earthquake swarm is not district from regular earthquakes in terms of their triggering process (Nakajima and Hasegawa 2023).

The Wakayama earthquake swarm is limited to a narrow (and shallow) depth range (5–10 km depth; Figs. 3 and 9), even though there is a continuous supply of slab-derived fluids throughout the seismogenic upper crust. Brittle deformation is required for the generation of earthquakes (e.g., Albaric et al. 2009); however, the frictional properties of rocks are also an important factor for seismogenesis (e.g., Scholz 1998). Maeda et al. (2021) estimated that the thickness of the seismogenic layer is 4–6 km for pelitic and mafic rocks beneath the Wakayama swarm and concluded that earthquakes occur in a limited depth range, where the friction parameter is negative, such that velocity-weakening behavior is expected. The observed depth range of the Wakayama swarm is

slightly deeper than the Matsushiro volcanic swarm (2–8 km depth) (Mogi 1988) but it is similar to the Yamagata–Fukushima earthquake swarm (6–10 km depth) in a volcanic area (Yoshida and Hasegawa 2018). Conversely, the depth range of the Wakayama swarm is shallower than the Noto earthquake swarm (10–15 km depth) in a non-volcanic area (Nakajima 2022). These observations suggest that heat flux beneath the Wakayama swarm is relatively high, despite a non-volcanic location, probably due to the concentrated upward migration of fluids from the uppermost mantle.

Conclusions

We systematically investigated the Wakayama earthquake swarm beneath the Kii peninsula in a non-volcanic area of Japan using the JMA earthquake catalog in the 2003–2020 period. The main conclusions of this study are as follows:

1. The average focal depth is 6.9 ± 1.9 km, and the b value is 0.96 ± 0.01 for the $M \geq 1$ earthquakes.
2. The swarm consists of small- to moderate-sized earthquakes with twelve $M \geq 4$ earthquakes, and the seismic activity occurs largely evenly in both time and space.
3. Most of the hypocenters in the northern part of the swarm activity occur along well-defined planes that dip to the west at 30°–45°, and a number of earthquakes are also distributed along conjugate, eastward-dipping fault planes.
4. Slab-derived fluids migrate to the Wakayama area through a northwestward-dipping permeable zone sandwiched by two impermeable bodies in the subduction direction of the PHS slab. The location of the Wakayama swarm is regulated by structural heterogeneities in the crust.
5. The persistent infiltration of huge amounts of fluid into individual crustal faults intermittently triggers aseismic slip, subsequently facilitating a cluster of earthquakes recognized as an earthquake swarm.
6. Observations of high $^3He/^4He$ ratios beneath the Kii peninsula, deep LFEs in the Osaka Bay, and Arima-type hot springs all point to the same origin, with the variations in these observations being manifested by different processes caused during the upward migration of slab-derived fluids.

This study has elucidated the important seismological features of the Wakayama swarm, thereby providing the opportunity to obtain a better understanding of this intriguing seismic activity, which occurs in a limited geographical area. Although this study can provide insights into the long-term earthquake activity across the Kii peninsula, the seismological analyses presented in this study only provide a present-day snapshot of subsurface structure, and they do not provide any information on the temporal evolution of slab-derived fluid migration to the Wakayama swarm. Petrological and geochemical observations and numerical simulations of fluid flow will resolve the time-dependent processes associated with this seismic activity.

Abbreviations

JMA	Japan Meteorological Agency
MTL	Median Tectonic Line

Supplementary Information

The online version contains supplementary material available at https://doi.org/10.1186/s40623-023-01807-6.

Additional file 1: Figure S1. (a) Earthquake distribution used in the tomographic inversion. Focal depths are color-coded. (b) Grid node configuration (blue crosses) and seismograph station locations (squares). Station colors represent the number of P-wave ray paths recorded at each station.

Additional file 2: Figure S2. Checkerboard resolution test results for P and S waves at 0, 5, 10, 15, 20, 25, 30, 40, and 60 km depth for checkerboard patterns that are assigned to (a) alternate grid nodes and (b) every two grid nodes.

Additional file 3: Figure S3. (a) P-wave and (b) S-wave absolute velocities and (c) V_p/V_s ratios at 10, 15, 20, 30, 40, and 60 km depth. Gray curves represent the iso-depth contour of the PHS slab at each depth. Regions with a deviated weight sum of > 1000 are shown. Hypocenter (black dots) and LFE (red dots) distributions are shown in (c).

Additional file 4: Figure S4. Vertical cross sections of the (a) P-wave and (a) S-wave absolute velocities and (c) V_p/V_s ratios along the seven profiles (A–G) shown on the inset map. Black dots and red circles denote the earthquakes and LFEs, respectively, within a 5-km-wide zone along each profile. Black dashed and black solid lines denote the Moho (Katsumata 2010) and upper surface of the PHS slab (Nakajima and Hasegawa 2007b; Hirose et al. 2008), respectively. Black bars on the surface represent the land areas.

Acknowledgements

We would like to thank D. Zhao for providing us with the tomography codes. Arrival-time data of earthquakes reported in the JMA-unified catalogue are used in this study. Discussion with A. Hasegawa was very fruitful.

Author contributions

JN designed the research, analyzed the data, and wrote the manuscript. All authors read and approved the final manuscript.

Funding

This work was supported by JSPS KAKENHI Grant Numbers JP20K20939 and JP21H01176 and by the Ministry of Education, Culture, Sports, Science and Technology of Japan, under its Earthquake and Volcano Hazards Observation and Research Program.

Availability of data and materials

We used arrival-time data of the JMA unified earthquake catalog and F-net focal mechanism solutions. These data are available from the web page of JMA (https://www.data.jma.go.jp/eqev/data/bulletin/index.html) and NIED (http://www.hinet.bosai.go.jp and https://www.fnet.bosai.go.jp/top.php?LANG=ja).

Declarations

Ethics approval and consent to participate
Not applicable.

Consent for publication
Not applicable.

Competing interests
The authors declare that they have no competing interests.

Author details
[1]Department of Earth and Planetary Sciences, School of Science, Tokyo Institute of Technology, Meguro-ku, Tokyo 152-8551, Japan.

Received: 4 November 2022 Accepted: 17 March 2023
Published online: 03 April 2023

References

Aki K, Koyanagi R (1981) Deep volcanic tremor and magma ascent mechanism Under Kilauea, Hawaii. J Geophys Res 86:7095–7109. https://doi.org/10.1029/JB086iB08p07095

Albaric J, Déverchère J, Petit C, Perrot C, Le Gall B (2009) Crustal rheology and depth distribution of earthquakes: Insights from the central and southern East African Rift System. Tectonophysics 468:28–41. https://doi.org/10.1016/j.tecto.2008.05.021

Arnulf AF, Bassett D, Harding AJ, Kodaira S, Nakanishi A, Moore G (2022) Upper-plate controls on subduction zone geometry, hydration and earthquake behaviour. Nat Geosci 15:143–148. https://doi.org/10.1038/s41561-021-00879-x

Aso N, Ohta K, Ide S (2011) Volcanic-like low-frequency earthquakes beneath Osaka Bay in the absence of a volcano. Geophys Res Lett 38:161–177. https://doi.org/10.1029/2011GL046935

Aso N, Ohta K, Ide S (2013) Tectonic, volcanic, and semi-volcanic deep low-frequency earthquakes in western Japan. Tectonophysics 600:27–40. https://doi.org/10.1016/j.tecto.2012.12.015

Bedford JD, Faulkner DR, Allen MJ, Hirose T (2021) The stabilizing effect of high pore-fluid pressure along subduction megathrust faults: evidence from friction experiments on accretionary sediments from the Nankai Trough. Earth Planet Sci Lett 574:117161. https://doi.org/10.1016/j.epsl.2021.117161

Cappa F, Scuderi MM, Collettini C, Guglielmi Y, Avouac JP (2019) Stabilization of fault slip by fluid injection in the laboratory and in situ. Sci Adv 5:1–9. https://doi.org/10.1126/sciadv.aau4065

Chen X, Shearer PM (2011) Comprehensive analysis of earthquake source spectra and swarms in the Salton Trough, California. J Geophys Res 116:1–17. https://doi.org/10.1029/2011JB008263

Christensen NI (1996) Poisson's ratio and crustal seismology. J Geophys Res 101:3139–3156. https://doi.org/10.1029/95JB03446

Danr P, De Barros L, Cappa F, Ampuero JP (2022) Prevalence of aseismic slip linking fluid injection to natural and anthropogenic seismic swarms. J Geophys Res Solid Earth 127:e2022JB025571. https://doi.org/10.1029/2022JB025571

Geological Survey of Japan, AIST (2022) Seamless digital geological map of Japan V2 1: 200,000. https://gbank.gsj.jp/seamless. Accessed 10 Mar 2023

Hasegawa A, Nakajima J (2017) Seismic imaging of slab metamorphism and genesis of intermediate-depth intraslab earthquakes. Prog Earth Planet Sci 4:12. https://doi.org/10.1186/s40645-017-0126-9

Hasegawa A, Yamamoto A (1994) Deep, low-frequency microearthquakes in or around seismic low-velocity zones beneath active volcanoes in northeastern Japan. Tectonophysics 233:233–252. https://doi.org/10.1016/0040-1951(94)90243-7

Hirose F, Nakajima J, Hasegawa A (2008) Three-dimensional seismic velocity structure and configuration of the Philippine Sea slab in southwestern Japan estimated by double-difference tomography. J Geophys Res 113:B09315. https://doi.org/10.1029/2007JB005274

Hua Y, Zhao D, Xu LX (2018) Age of the subducting Philippine Sea slab and mechanism of low-frequency earthquakes. Geophys Res Lett 45:2303–2310. https://doi.org/10.1002/2017GL076531

Isozaki Y, Maruyama S, Furuoka F (1990) Accreted oceanic materials in Japan. Tectonophysics 181:179–205. https://doi.org/10.1016/0040-1951(90)90016-2

Kato A, Sakai S, Iidaka T, Iwasaki T, Hirata N (2010) Non-volcanic seismic swarms triggered by circulating fluids and pressure fluctuations above a solidified diorite intrusion. Geophys Res Lett 37:161–177. https://doi.org/10.1029/2010GL043887

Kato A, Saiga A, Takeda T, Iwasaki T, Matsuzawa T (2014) Non-volcanic seismic swarm and fluid transportation driven by subduction of the Philippine Sea slab beneath the Kii Peninsula, Japan. Earth Planets Space 66:86. https://doi.org/10.1186/1880-5981-66-86

Katsumata A (2010) Depth of the Moho discontinuity beneath the Japanese islands estimated by traveltime analysis. J Geophys Res 115:B04303. https://doi.org/10.1029/2008JB005864

Keranen KM, Weingarten M, Abers GA, Bekins BA, Ge S (2014) Sharp increase in central Oklahoma seismicity since 2008 induced by massive wastewater injection. Science 345:448–451. https://doi.org/10.1126/science.1255802

Kita S, Matsubara M (2016) Seismic attenuation structure associated with episodic tremor and slip zone beneath Shikoku and the Kii peninsula, southwestern Japan, in the Nankai subduction zone. J Geophys Res Solid Earth 121:1962–1982. https://doi.org/10.1002/2015JB012493

Kusuda C, Iwamori H, Nakamura H, Kazahaya K, Moikawa N (2014) Arima hot spring waters as a deep-seated brine from subducting slab. Earth Planets Space 66:1–13. https://doi.org/10.1186/1880-5981-66-119

Maeda S, Matsuzawa T, Toda S, Yoshida K, Katao H (2018) Complex microseismic activity and depth-dependent stress field changes in Wakayama, southwestern Japan. Earth Planets Space 70:21. https://doi.org/10.1186/s40623-018-0788-6

Maeda S, Toda S, Matsuzawa T, Otsubo M, Matsumoto T (2021) Influence of crustal lithology and the thermal state on microseismicity in the Wakayama region, southern Honshu, Japan. Earth Planets Space 73:173. https://doi.org/10.1186/s40623-021-01503-3

Matsubaya O, Sakai H, Kusachi I, Satake H (1973) Hydrogen and oxygen isotopic ratios and major element chemistry of Japanese thermal water systems. Geochem J 7:123–151. https://doi.org/10.2343/geochemj.7.123

Matsumoto T, Kawabata T, Matsuda JI, Yamamoto K, Mimura K (2003) $^{3}He/^{4}He$ ratios in well gases in the Kinki district, SW Japan: surface appearance of slab-derived fluids in a non-volcanic area in Kii Peninsula. Earth Planet Sci Lett 216:221–230. https://doi.org/10.1016/S0012-821X(03)00479-5

Matsunami K, Nakamura M (2004) Seismic attenuation in a nonvolcanic swarm region beneath Wakayama, southwest Japan. J Geophys Res 109:161–177. https://doi.org/10.1029/2003JB002758

Mizoue M, Nakamura M, Seto N, Ishiketa Y, Yokota T (1983) Three-layered distribution of microearthquakes in relation to focal mechanism variation in the Kii peninsula, southwestern Honshu, Japan. Bull Earthq Res Inst 58:287–310

Mogi K (1988) The mechanism of the occurrence of the Matsushiro earthquake swarm in central Japan and its relation to the 1964 Niigata earthquake. Tectonophysics 159:109–119. https://doi.org/10.1016/0040-1951(89)90173-X

Morikawa N, Kazahaya K, Takahashi M, Inamura A, Takahashi HA, Yasuhara M, Ohwada M, Sato T, Nakama A, Handa H, Sumino H, Nagao K (2016) Widespread distribution of ascending fluids transporting mantle helium in the fore-arc region and their upwelling processes: noble gas and major element composition of deep groundwater in the Kii Peninsula, southwest Japan. Geochim Cosmochim Acta 182:173–196. https://doi.org/10.1016/j.gca.2016.03.017

Nakajim J (2022) Crustal structure beneath earthquake swarm in the Noto peninsula, Japan. Earth Planets Space 74:160. https://doi.org/10.1186/s40623-022-01719-x

Nakajima J, Hasegawa A (2007a) Tomographic evidence for the mantle upwelling beneath southwestern Japan and its implications for arc magmatism. Earth Planet Sci Lett 254:90–105. https://doi.org/10.1016/j.epsl.2006.11.024

Nakajima J, Hasegawa A (2007b) Subduction of the Philippine Sea plate beneath southwestern Japan: slab geometry and its relationship to arc magmatism. J Geophys Res 112:B08306. https://doi.org/10.1029/2006JB004770

Nakajima J, Hasegawa A (2016) Tremor activity inhibited by well-drained conditions above a megathrust. Nat Commun 7:13863. https://doi.org/10.1038/ncomms13863
Nakajima J, Hasegawa A (2023) Prevalence of repeating earthquakes in the continental crust and subducting slabs: triggering of earthquakes by aseismic slip. J Geophys Res Solid Earth 128:e2022JB024667. https://doi.org/10.1029/2022JB024667
Nakajima J, Matsuzawa T, Hasegawa A, Zhao D (2001) Three-dimensional structure of Vp, Vs, and Vp/Vs beneath northeastern Japan: implications for arc magmatism and fluids. J Geophys Res 106:21843–21857. https://doi.org/10.1029/2000JB000008
Oikawa G, Aso N, Nakajima J (2021) Depth dependent focal mechanisms of volcanic deep low-frequency earthquakes in Northeast Japan. J Geophys Res Solid Earth 126:e2021JB022666. https://doi.org/10.1029/2021JB022666
Omuralieva AM, Hasegawa A, Matsuzawa T, Nakajima J, Okada T (2012) Lateral variation of the cutoff depth of shallow earthquakes beneath the Japan Islands and its implications for seismogenesis. Tectonophysics 518–521:93–105. https://doi.org/10.1016/j.tecto.2011.11.013
Oth A (2013) On the characteristics of earthquake stress release variations in Japan. Earth Planet Sci Lett 377–378:132–141. https://doi.org/10.1016/j.epsl.2013.06.037
Peacock SM (2009) Thermal and metamorphic environment of subduction zone episodic tremor and slip. J Geophys Res 114:161–177. https://doi.org/10.1029/2008JB005978
Petukhin A, Tagawa T (2007) High Seismic Attenuation in the Reflective Layers of the Philippine Sea Subduction Zone, Japan. In: Eichlberger J, Gordeev E, Izbekov P, Kasahara M, Lees J (eds) Geophys Monogr 172:117–126. https://doi.org/10.1029/172GM11
Salah MK, Zhao D (2003) 3-D seismic structure of Kii Peninsula in southwest Japan: evidence for slab dehydration in the forearc. Tectonophysics 364:191–213. https://doi.org/10.1016/S0040-1951(03)00059-3
Sano Y, Nakajima J (2008) Geographical distribution of 3He/4He ratios and seismic tomography in Japan. Geochem J 42:51–60. https://doi.org/10.2343/geochemj.42.51
Sano Y, Wakita H (1985) Geographical distribution of ^{3}He/^{4}He ratios in Japan: implications for arc tectonics and incipient magmatism. J Geophys Res 90:8729–8741. https://doi.org/10.1029/JB090iB10p08729
Sano Y, Kameda A, Takahata N, Yamamoto J, Nakajima J (2009) Tracing extinct spreading center in SW Japan by helium-3 emanation. Chem Geol 266:50–56. https://doi.org/10.1016/j.chemgeo.2008.10.020
Scholz CH (1998) Earthquakes and friction laws. Nature 391:37–42. https://doi.org/10.1038/34097
Seno T, Zhao D, Kobayashi Y, Nakamura M (2001) Dehydration of serpentinized slab mantle: seismic evidence from southwest Japan. Earth Planets Space 53:861–871
Shelly DR, Hill DP, Massin F, Farrell J, Smith RB, Taira T (2013) A fluid-driven earthquake swarm on the margin of the Yellowstone caldera. J Geophys Res 118:4872–4886. https://doi.org/10.1002/jgrb.50362
Takei Y (2002) Effect of pore geometry on V_P/V_S: from equilibrium geometry to crack. J Geophys Res 107:2043. https://doi.org/10.1029/2001JB000522
Tanaka A, Yamano M, Yano Y, Sasada M (2004) Geothermal gradient and heat flow data in and around Japan (I): appraisal of heat flow from geothermal gradient data. Earth Planets Space 56:1191–1194. https://doi.org/10.1186/BF03353339
Terakawa T, Matsu'ura M (2010) The 3-D tectonic stress fields in and around Japan inverted from centroid moment tensor data of seismic events. Tectonics 29:6008. https://doi.org/10.1029/2009TC002626
Uchide T, Shiina T, Imanishi K (2022) Stress map of Japan: detailed nationwide crustal stress field inferred from focal mechanism solutions of numerous microearthquakes. J Geophys Res Solid Earth 127:4036. https://doi.org/10.1029/2022JB024036
Uehara D, Kakuta C, Kudo T, Umeda K, Ogawa Y, Tanase A, Takeda M, Chiba A, Kikuchi A, Tagiyama T (2005) Geothermal structure of the southern part of the Kii peninsula estimated from the gravity anomaly and the deep resistivity structure. Zisin 57:245–255 (**in Japanese with English abstract**)
Ueno H, Hatakeyama S, Aketagawa T, Funasaki J, Hamada N (2002) Improvement of hypocenter determination procedures in the Japan Meteorological Agency. Quart J Seism 65:123–134 (**in Japanese with English abstract**)
Umeda K, Sakagawa Y, Ninomiya A, Asamori K (2007) Relationship between helium isotopes and heat flux from hot springs in a non-volcanic region, Kii Peninsula, southwest Japan. Geophys Res Lett 34:161–177. https://doi.org/10.1029/2006GL028975
Waldhauser F, Ellsworth WL (2000) A double-difference earthquake location algorithm: method and application to the Northern Hayward Fault, California. Bull Seismol Soc Am 90:1353–1368. https://doi.org/10.1785/0120000006
Watanabe T, Kasami H, Ohshima S (2007) Compressional and shear wave velocities of serpentinized peridotites up to 200 MPa. Earth Planets Space 59:233–244
Wiemer S, Wyss M (2000) Minimum magnitude of completeness in earthquake catalogs: examples from Alaska, the Western United States, and Japan. Bull Seismol Soc Am 90:859–869. https://doi.org/10.1785/0119990114
Yamasaki T, Seno T (2003) Double seismic zone and dehydration embrittlement of the subducting slab. J Geophys Res 108:2212. https://doi.org/10.1029/2002JB001918
Yamauchi M, Hirahara K, Shibutani T (2003) High resolution receiver function imaging of the seismic velocity discontinuities in the crust and the uppermost mantle beneath southwest Japan. Earth Planets Space 55:59–64. https://doi.org/10.1186/BF03352463
Yoshida K, Hasegawa A (2018) Hypocenter migration and seismicity pattern change in the Yamagata- Fukushima border, NE Japan, caused by fluid movement and pore pressure variation. J Geophys Res Solid Earth 123:5000–5017. https://doi.org/10.1029/2018JB015468
Yoshida A, Takayama H (1992) Correlation of seismic activities in the circumferential areas of the Kinki Triangle and its tectonic significance. J Geogr 101:327–335 (**in Japanese with English abstract**)
Yoshida A, Hosono K, Takayama H, Kobayashi A, Maeda K (2011) Seismic and geodetic evidence for the existence of hot materials beneath the Wakayama swarm activity, southwestern Japan. Tectonophysics 510:124–131. https://doi.org/10.1016/j.tecto.2011.06.023
Yoshioka S, Toda M, Nakajima J (2008) Regionality of deep low-frequency earthquakes associated with subduction of the Philippine Sea plate along the Nankai Trough, southwest Japan. Earth Planet Sci Lett 272:189–198. https://doi.org/10.1016/j.epsl.2008.04.039
Zhao D, Hasegawa A, Horiuchi S (1992) Tomographic imaging of P and S wave velocity structure beneath Northeastern Japan. J Geophys Res 97:19909–19928. https://doi.org/10.1029/92JB00603

Publisher's Note